



Article

Identifying the Degradation Mechanism in Commercial Lithium Rechargeable Batteries via High-Energy X-ray Compton Scattering Imaging

Kosuke Suzuki ^{1,*}, Yuji Otsuka ¹, Naruki Tsuji ², Kazushi Hoshi ¹, Yoshiharu Sakurai ² and Hiroshi Sakurai ¹

¹ Faculty of Science and Technology, Gunma University, 1-5-1 Tenjin-cho, Kiryu, Gunma 376-8515, Japan; t201d016@gunma-u.ac.jp (Y.O.); hoshi@gunma-u.ac.jp (K.H.); sakuraih@gunma-u.ac.jp (H.S.)

² Japan Synchrotron Radiation Research Institute (JASRI), SPring-8, Sayo, Hyogo 679-5198, Japan; ntsuji@spring8.or.jp (N.T.); sakurai@spring8.or.jp (Y.S.)

* Correspondence: kosuzuki@gunma-u.ac.jp; Tel.: +81-277-30-1714

Received: 14 July 2020; Accepted: 20 August 2020; Published: 24 August 2020



Abstract: Synchrotron-based high-energy X-ray Compton scattering imaging is a promising technique for non-destructively and quantitatively investigating commercialized lithium rechargeable batteries. We apply the Compton scattering imaging technique to commercial coin-type lithium rechargeable cells (VL2020) to non-destructively identify the degradation mechanism of the cell. The correlations between the Compton scattering intensity and line-shape of the Compton scattering X-ray energy spectrum (S-parameter) obtained from this technique produce unique distributions that characterize the aged cell. These distributions in the aged cell indicate that the stable phase of the anode formed through the overvoltage charge–discharge cycle. This stable phase prevents lithium reactions, producing microbubbles with the decomposition of the electrolyte.

Keywords: lithium rechargeable battery; LiAl alloy; degradation mechanism; Compton scattering imaging; high-energy synchrotron X-ray; non-destructive analysis

1. Introduction

The demand for renewable energy from natural sources, like sunlight and wind, is rapidly increasing all over the world. The development of high-performance storage devices, like lithium rechargeable batteries, is important for stably using these renewable energies [1]. The lithium rechargeable batteries, as storage devices, must be high capacity, safe to use, and have a long lifetime. Increasing the size of the cell is important to achieve high capacity; observing the lithium reaction in situ and in operando in a local region in commercialized rechargeable cells is important for a long lifetime and ensuring safety. So far, various experimental techniques for observing lithium rechargeable batteries have been reported using synchrotron X-rays and neutron and electron particle beams, and also, the electronic and geometric structures of the materials have been characterized using various length and time scales [2]. Recent cryo-electron microscopy techniques have achieved characterization of the electrode materials toward the realization of next-generation batteries [3–6]. These studies clearly visualize lithium dendrites.

Among them, Compton scattering imaging is a promising technique for non-destructively observing the structure of the matter in a local region [7]. Compton scattering imaging is an experimental technique that uses high-energy X-rays. High-energy X-rays have high matter penetration power, which allows large-scale non-destructive construction measurement. High-energy X-rays can be used to measure light elements, as incoherent scattering (Compton) effects are enhanced with the

interaction between photons and electrons. These advantages of Compton scattering imaging have been applied to a variety of fields, including the medical and security fields [8,9]. However, these studies have been mainly performed using a proportional counter, such as a flat-panel detector and linear array detectors, and do not analyze the energy of Compton scattering X-ray photons.

We have been developing a method for non-destructively and quantitatively monitoring lithium ions in the cell using Compton scattering imaging combined with a synchrotron-based high-energy X-ray and energy-dispersive-type detector. Thus far, we have applied this technique to the commercial lithium primary cell CR2032 under discharge, where, by measuring the Compton scattering intensities, the migration of lithium ions from the anode to the cathode was visualized as the difference in the electron density, and the structural changes due to the volume expansion of the electrodes were revealed [10]. These results showed that the difference in the Compton scattering intensities produced by the difference in the electron density enabled the non-destructive estimation of the matter in the cell. Additionally, the change in the lithium concentration with the charge and discharge of the cell could be quantitatively determined from the line-shape of the Compton scattering X-ray energy spectrum, called the Compton profile, using line-shape parameter analysis, also known as S-parameter analysis [11]. Lithium compositions in the commercial lithium rechargeable battery VL2020 at the cathode and anode were simultaneously obtained while cycling [12]. S-parameter analysis was also used to show the dependency of the cycle rate on the lithiation state in the VL2020 cell [13] and to non-destructively identify the difference between the fresh and aged 18650-type cells with micrometer-scale spatial resolution [14]. However, the Compton scattering X-ray intensity and the S-parameter analysis were performed individually. Therefore, in this study, we non-destructively identified the degradation state of the commercial coin-type cell by combining both the Compton scattering X-ray intensities and S-parameter analysis methods.

2. Experimental

In this study, we use a commercial coin-type lithium rechargeable battery (VL2020, Panasonic Corporation, Osaka, Japan). The VL2020 is composed of a V_2O_5 cathode, an olefin-based non-woven fabric separator, an LiAl alloy anode, and a dimethoxyethane electrolyte. Although these cathode and anode materials are different from typical lithium-ion batteries used in the industry today, the V_2O_5 and LiAl alloy are still extensively studied for electrodes. The features of V_2O_5 cathodes are low cost, abundance, and having the possibility for high capacity. Here, the theoretical capacities of V_2O_5 , $LiCoO_2$, $LiMn_2O_4$, and $LiFePO_4$ are 294 mAhg^{-1} , 274 mAhg^{-1} , 148 mAhg^{-1} , and 170 mAhg^{-1} , respectively. The V_2O_5 of micro- and nano-structures have demonstrated good cycle performance and rate properties [15–17]. V_2O_5 is also considered as a cathode material for next-generation Al-ion [18] and Mg-ion batteries [19]. The LiAl alloy anodes are attracting attention in the battery industry. The LiAl alloys have potential as anodes for lithium-oxygen batteries and have been reported to have high cycle stability [20]. The thicknesses of the cathode and anode are $800 \mu\text{m}$ and approximately $300 \mu\text{m}$, respectively. The nominal voltage and capacity of the cell are 3 V and 20 mAh, respectively. The cut-off voltages are 2.5 and 3.5 V.

To analyze the degraded state of the cell, an unused cell (called a fresh cell) and a used cell (called an aged cell) were used. The aged cell was prepared by cycling the cell 170 times at room temperature. During the cycling process, the cell repeatedly charged and discharged with a constant current (CC) of 10 mA. A reference cycle was performed at 10 cycle intervals. In the reference cycle, the cell was charged with a CC of 2 mA until the 3.5 V cut-off voltage was reached, and the charging was continued 3 h in constant voltage (CV) mode at 3.5 V. Afterward, the discharge was performed with a CC of 2 mA until the 2.5 V cut-off voltage was reached. We confirmed that the capacity became almost 0 mAh after 170 cycles, as shown in Figure 1b.

Compton scattering experiments were conducted at BL08Wof the Synchrotron Facility, SPring-8, Hyogo, Japan. The experimental setup is shown in Figure 1c. The incident X-rays emitted from a multipole wiggler were monochromatized to 114.56 keV using bend-type Si(400) crystal. X-ray energy

spectra along the scattering angle of 90 degrees were measured using nine segments of a pure Ge solid-state detector (SSD). These nine detectors were adjusted by the collimator slit to observe the same region in the sample cell. The observation region in the cell was limited by the incident and collimator slits. The sizes of these incident and collimator slits were $20 \times 500 \mu\text{m}^2$ and $500 \mu\text{m}$ in diameter, respectively. The cell was set on a movable stage, which had a function adjustment system using the x , y , and z positions of the sample cell and the θ , azimuth, and tilt angles. The Compton scattering X-ray energy spectrum was measured using scanning incident X-rays along the vertical (z) and horizontal (x) directions of the cell. The scanning area was 0.8–1 mm in height and 5 mm in width, which corresponded from the lower end of the cathode to the end of the anode on the z -direction. The measurement time at one position was 30 s.

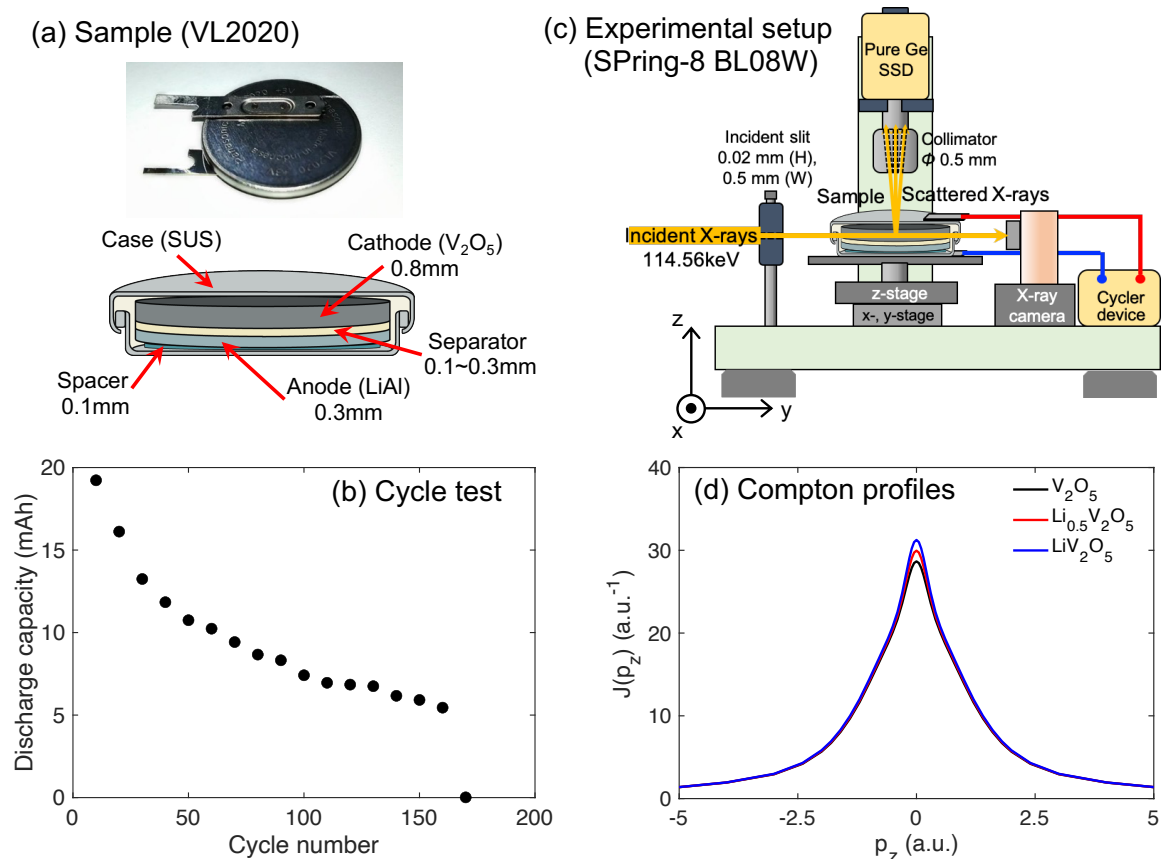


Figure 1. (a) Picture and schematic image of a commercial coin-type lithium rechargeable cell VL2020. (b) The cycle dependency of the discharge capacity in the VL2020 cell. This study uses two cells with zero cycles and after 170 cycles. (c) The experimental setup of the Compton scattering imaging system at BL08W of SPring-8. (d) Theoretical Compton profiles of $\text{Li}_x\text{V}_2\text{O}_5$ ($x = 0, 0.5, \text{ and } 1$) obtained from the Hartree–Fock calculations.

The obtained X-ray energy spectrum was analyzed using two methods: Compton scattering X-ray intensity and the S-parameter. The Compton scattering X-ray intensity, dN , is calculated as [21]:

$$dN = \Phi_0 t_1 t_2 \rho_e dV \frac{d\sigma_{\text{KN}}}{d\Omega}, \quad (1)$$

where Φ_0 is the photon flux of the incident X-rays; t_1 and t_2 are the path length of the incident and scattering X-rays in the target matter, respectively; ρ_e is the average electron density over the probing volume; dV is the probing volume; and $d\sigma_{\text{KN}}/d\Omega$ is the Klein–Nishina differential cross-section. Experimentally, dN is given by the area of the Compton scattering X-ray energy spectrum. dN depends on t_1 , t_2 , and ρ_e . When the X-ray path length can be treated as constant, the Compton scattering X-ray

intensity is proportional to the electron density ρ_e . Therefore, Compton scattering intensity has been used for densitometry [21] and imaging [7,22], and the analysis of Compton scattering X-ray intensity allows the identification of the matter at the local region in the cell.

The S-parameter is a parameter that characterizes the modification of the Compton scattering X-ray energy spectrum with lithium insertion. Figure 1d shows the Compton scattering X-ray energy spectrum, the so-called Compton profile, of $\text{Li}_x\text{V}_2\text{O}_5$ (lithium concentration $x = 0, 0.5, \text{ and } 1$) obtained from Hartree–Fock calculations [23]. The peak height, which is seen to increase with increasing lithium concentration, demonstrates the sensitivity of the profile to the lithium concentration. A previous study clarified that there is linearity between the experimental S-parameter and lithium concentration obtained from inductively-coupled plasma (ICP) analysis [11]. Therefore, the S-parameter allows us to quantitate the lithium concentration in the electrode non-destructively. The Compton profile, $J(p_z)$, is related to the ground-state electron momentum density $\rho(\mathbf{p})$ in the momentum space via the following double integral [24]:

$$J(p_z) = \iint \rho(\mathbf{p}) dp_x dp_y, \quad (2)$$

where $\mathbf{p} = (p_x, p_y, p_z)$ is the electron momentum. $\rho(\mathbf{p})$ is given by [25,26]:

$$\rho(\mathbf{p}) = (2\pi)^{-3/2} \sum_j n_j \left| \int \Psi_j(\mathbf{r}) \exp(-i\mathbf{p} \cdot \mathbf{r}) d\mathbf{r} \right|^2, \quad (3)$$

where $\Psi_j(\mathbf{r})$ is the wave function of an electron in the j -state and n_j is the electron occupation. The index j covers all constituent atoms and orbitals. $J(p_z)$ is directly linked to the wave function in real space, and the line-shape of $J(p_z)$ changes depending on the chemical element. These features have also been used to identify electronic structures and redox orbitals in the electrode reaction through the combination with first-principle calculations and have successfully visualized the redox orbitals of cathode materials [27–30]. The S-parameter is defined as [11]:

$$S = \frac{\int_{-d}^d J(p_z) dp_z}{\int_{-l}^d J(p_z) dp_z + \int_d^l J(p_z) dp_z}, \quad (4)$$

where parameters d and l define the range of low- and high-momentum regions, respectively, dividing the dominant and inconspicuous lithium regions. We used $d = 1$ atomic units (a.u.) and $l = 5$ a.u. These were determined by comparing fully charged and discharged Compton scattering X-ray energy spectra as reported previously [14].

3. Results and Discussion

The Compton scattering X-ray energy spectra obtained from the cathode, separator, and anode of the fresh cell are shown in Figure 2a. The area of these energy spectra was normalized to the same value to clarify the line-shape of each energy spectrum. The x-axis, p_z in Figure 2a, represents the electron momentum along the z-direction, which experimentally corresponds to the scatter vector direction. p_z is given by [24]:

$$\frac{p_z}{mc} = \frac{E_0 - E_i + (E_i E_0 / mc^2) (1 - \cos \theta)}{\sqrt{E_i^2 + E_0^2 - 2E_i E_0 \cos \theta}}, \quad (5)$$

where mc is $1/\alpha$ and α is the fine structure constant (as we used atomic units following the conventions of X-ray spectroscopy). E_0 and E_i are the incident and scattering X-ray energy, respectively; mc^2 is the rest mass energy of the electron; and θ is a scattering angle. The energy spectrum obtained from the separator has a narrow distribution, and the energy spectrum obtained from the anode has a broad distribution, as shown in Figure 2a.

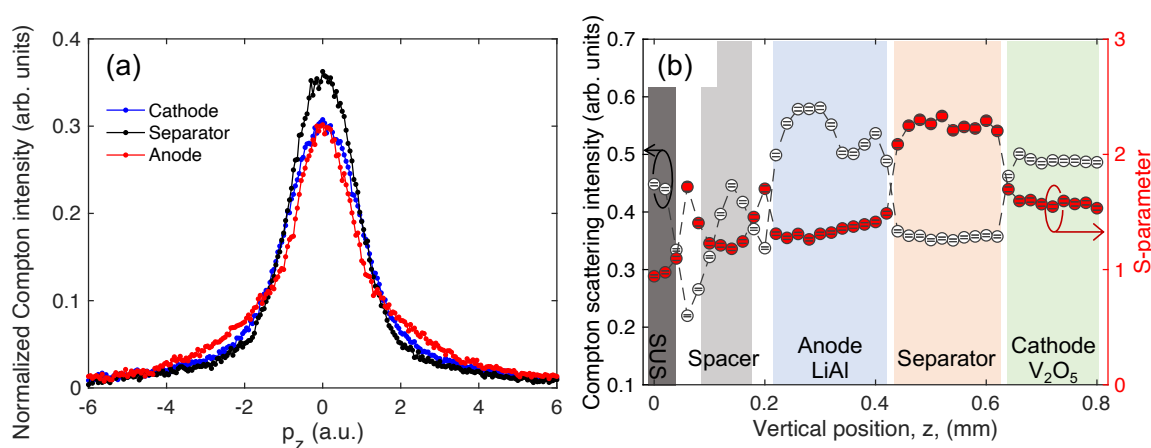


Figure 2. (a) Compton scattering X-ray energy spectrum obtained from the cathode (blue line), separator (black line), and anode (red line) of the fresh VL2020 cell. (b) The internal structure of the cell obtained from the Compton scattering intensity (white filled circle) and S-parameter (red filled circle). The background colors correspond to the regions of each component of the cell.

Figure 2b shows the internal structure of the fresh VL2020 cell in the discharged state observed using Compton scattering intensity and the S-parameter. These data were obtained from the Compton scattering X-ray energy spectrum, which was measured using the scanning incident X-rays from the lower end of the cathode to the end of the anode. The Compton scattering intensities were obtained by normalizing the number of photons of the Compton scattering X-rays by the number of photons of the incident X-rays, which were measured using an ion-chamber. The measurement time was 30 s at each point. The background colors in Figure 2b indicate the region of each component of the cell. The regions at $0 \text{ mm} \geq z < 0.04 \text{ mm}$, $0.08 \text{ mm} < z < 0.18 \text{ mm}$, $0.21 \text{ mm} < z < 0.42 \text{ mm}$, $0.43 \text{ mm} < z < 0.64 \text{ mm}$, and $0.65 \text{ mm} < z \leq 0.8 \text{ mm}$ correspond to the stainless steel outer casing, spacer, anode, separator, and cathode, respectively. The Compton scattering intensity interestingly indicated that the anode had a two-layer structure. Although the Compton scattering intensity and S-parameter had opposite trends in this cell as shown in Figure 2b, we can non-destructively identify the inner structure of the cell using both the Compton scattering intensity and S-parameter.

Figure 3a,b depicts the Compton scattering intensity distribution, and Figure 3c,d is the S-parameter distribution of the charged and discharged states in the fresh cell, respectively. The state of charge on the cell changed by a constant current of 2 mA. The separator position shifted about 80 μm toward the cathode direction by charging the fresh cell in both the Compton scattering intensity and S-parameter distributions. This shift in the separator position is caused by the volume expansion of the anode because the lattice volume of the LiAl alloy expands about 95% compared with that of Al by inserting lithium [31]. Therefore, in the Compton scattering intensity distribution, the intensity of the anode region decreased by charging the cell despite the average electron density increase with the lithium insertion. The S-parameter intensity increased because lithium ions moved to the anode during charge. The averaged S-parameter at the cathode and anode in the charged and discharged states and the corresponding lithium composition are summarized in Table 1. The lithium composition was determined using the calibration curve between the S-parameter and lithium composition, which was measured previously using inductively-coupled plasma (ICP) analysis. Here, the S-parameter obtained from the charged state in the cathode was normalized by the lithium composition in the charged state of the cathode obtained from the ICP analysis, and the S-parameter obtained from the discharged state in the anode was normalized by the lithium composition in the discharged state of the anode obtained from the ICP analysis. The details of the calibration curve were reported previously [12]. By charging the cell, the S-parameter of the anode increases approximately 3.18%, and that of the cathode decreases

approximately 1.25%. Here, the lithium composition on the cathode changes from 0.124 ± 0.190 to 0.723 ± 0.190 with the discharge; the lithium composition on the anode changes from 0.046 ± 0.031 to 0.270 ± 0.031 with the charge. From the above, we observe a clear variation in the fresh cell in the charged and discharged states via the Compton scattering intensity and S-parameter.

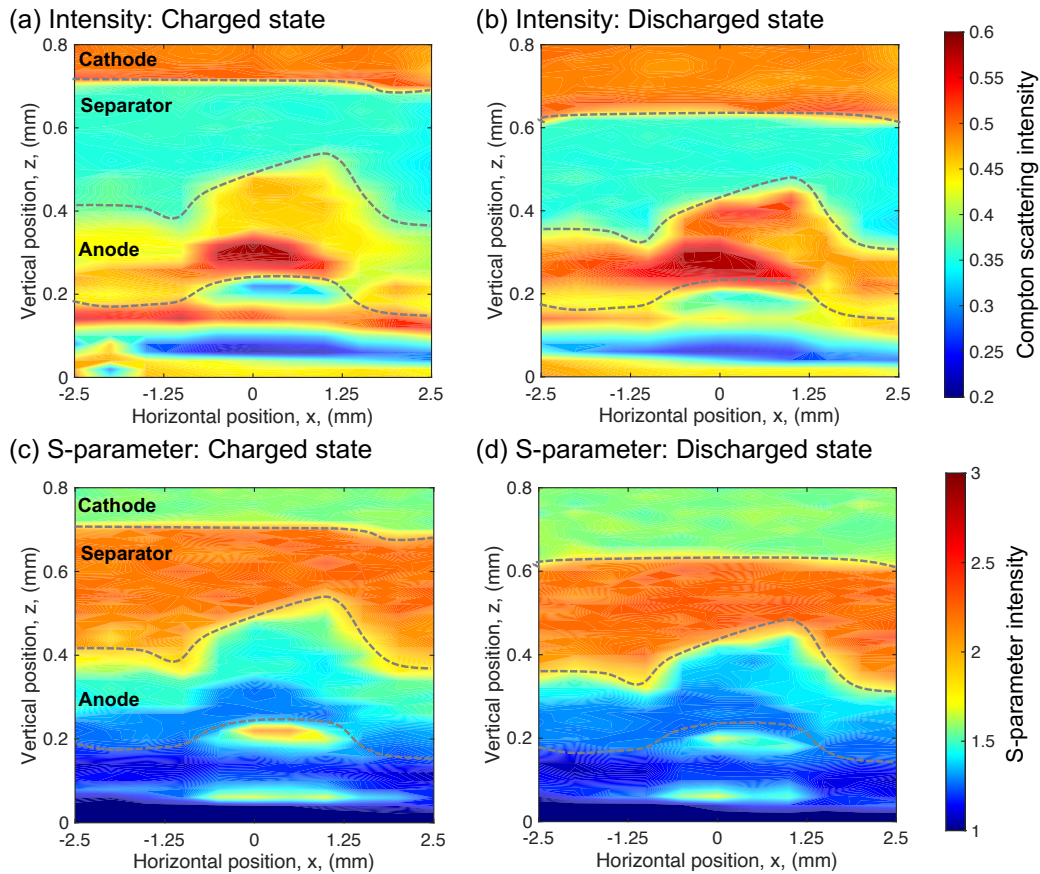


Figure 3. In the fresh cell: (a) The Compton scattering intensity distribution in the charged state. (b) The Compton scattering intensity distribution in the discharged state. (c) The S-parameter distribution in the charged state. (d) The S-parameter distribution in the discharged state.

Table 1. The averaged S-parameter and corresponding lithium composition in the charged and discharged states in the fresh cell.

	Averaged S-Parameter		Lithium Composition	
	Charged State	Discharged State	Charged State	Discharged State
Cathode	1.574 ± 0.006	1.592 ± 0.006	0.124 ± 0.095	0.723 ± 0.095
Anode	1.392 ± 0.006	1.349 ± 0.006	0.270 ± 0.029	0.046 ± 0.031

On the other hand, the aged cell produces a different response with charge and discharge compared with the fresh cell. Figure 4a,b depicts the Compton scattering intensity distribution, and Figure 4c,d depicts the S-parameter distribution of the charged and discharged states in the aged cell, respectively. The state of charge on the cell changed by a constant current with 2 mA. However, in the aged cell, a clear variation in the distribution at the charged and discharged states is not observed in both the Compton scattering intensity and S-parameter distributions. The averaged S-parameter and corresponding lithium composition of both electrodes do not show a significant change, as summarized in Table 2. Comparing these distributions of the aged cell with those of the fresh cell, we observe that the anode expanded and the separator shrank in the aged cell. Hence, the region under the anode also shows a difference in distribution. Hamon et al. reported that the capacity loss of the cell is induced by

the expansion of the LiAl alloy electrode [32]. Interestingly, a region with a low Compton scattering intensity and high S-parameter value appears near the interface between the cathode and separator.

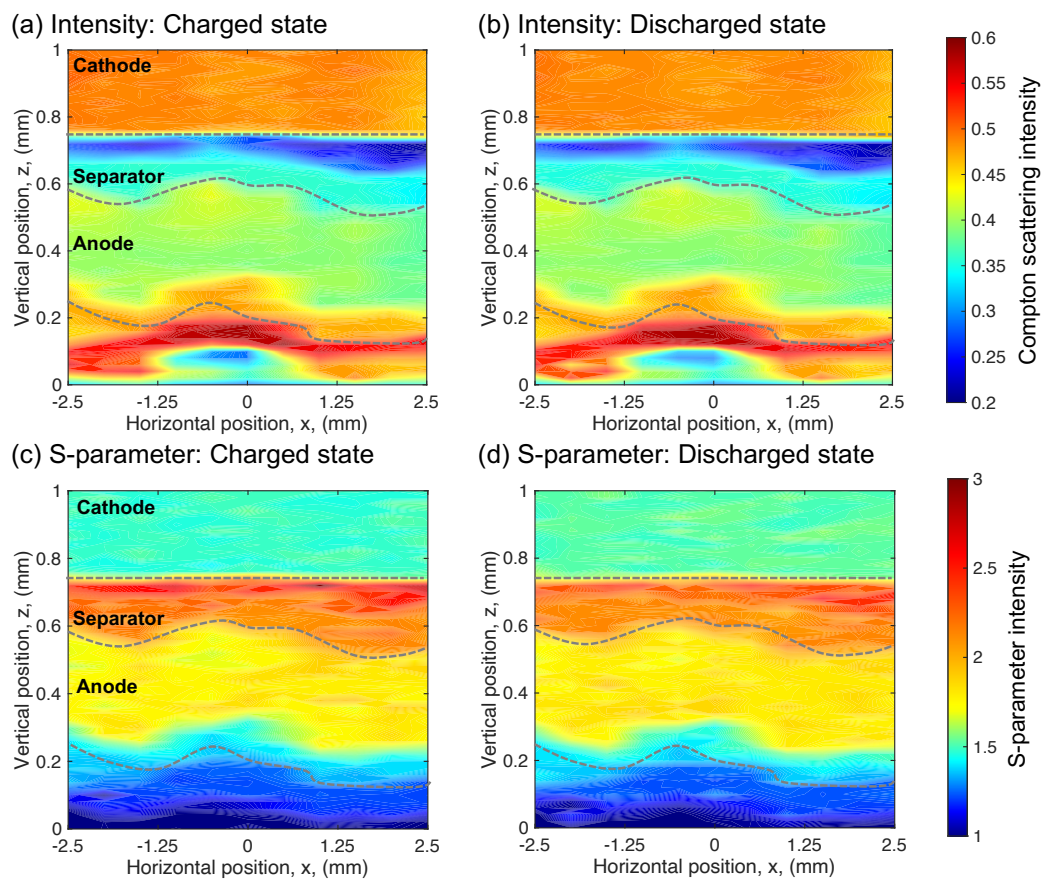


Figure 4. In the aged cell: (a) The Compton scattering intensity distribution in the charged state. (b) The Compton scattering intensity distribution in the discharged state. (c) The S-parameter distribution in the charged state. (d) The S-parameter distribution in the discharged state.

Table 2. The averaged S-parameter and corresponding lithium composition in the charged and discharged states in the aged cell.

	Averaged S-Parameter		Lithium Composition	
	Charged State	Discharged State	Charged State	Discharged State
Cathode	1.590 ± 0.005	1.590 ± 0.005	0.124 ± 0.077	0.130 ± 0.078
Anode	1.785 ± 0.005	1.783 ± 0.006	0.055 ± 0.022	0.046 ± 0.023

The correlation between the Compton scattering intensity and the S-parameter in the fresh and aged cells is shown in Figure 5, depicting the change in the internal structure of the aged cell. In the fresh cell, the distributions between the Compton scattering intensity and S-parameter in the charged state of the cathode, separator, and anode are concentrated at the region around 0.5 in the Compton scattering intensity and 1.5 for the S-parameter, around 0.35 in the Compton scattering intensity and 2.3 for the S-parameter, and around 0.45 in the Compton scattering intensity and 1.4 for the S-parameter, respectively, as shown in Figure 5a. The distributions in the discharged state of the fresh cell display the same trends as the charged state, as shown in Figure 5b. By charging the fresh cell, the barycenter position of the anode distributions shifts from 0.5014 ± 0.0002 to 0.4589 ± 0.0001 in the Compton scattering intensity and from 1.3510 ± 0.0017 to 1.3977 ± 0.0017 in the S-parameter. By discharging the cell, the barycenter position of the cathode distributions shifts from 0.4937 ± 0.0001 to 0.4896 ± 0.0001

in the Compton scattering intensity and from 1.5723 ± 0.0014 to 1.5928 ± 0.0019 in the S-parameter. These results correspond to Figure 3.

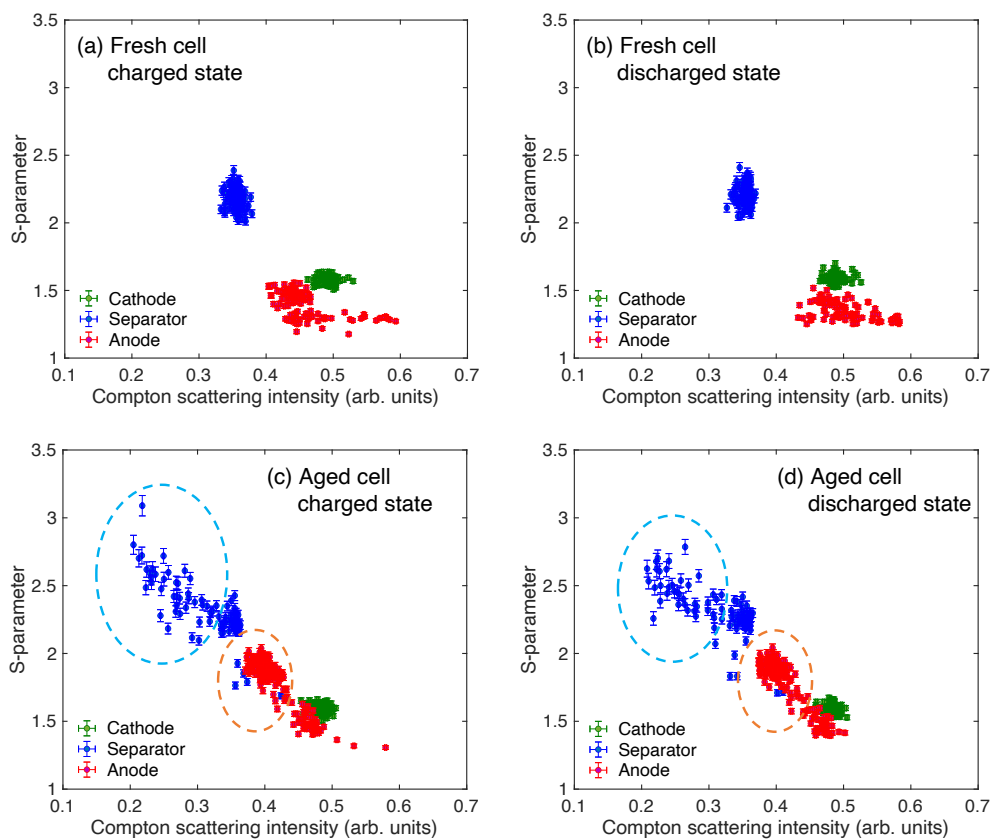


Figure 5. The correlation between the Compton scattering intensity and S-parameter. The data obtained from the cathode, anode, and separator are shown in green, red, and blue circles, respectively. (a) The charged state of the fresh cell. (b) The discharged state of the fresh cell. (c) The charged state of the aged cell. (d) The discharged state of the aged cell. The distribution regions characterizing the aged cell are highlighted in blue and orange dotted line circles in Figure 5c,d.

The distributions between the Compton scattering intensity and S-parameter in the aged cell are different from those of the fresh cell, as shown in Figure 5c,d. The barycenter positions of the cathode and anode distributions do not show a significant change between the charged and discharged states. These values in the cathode of the charged and discharged states are 0.4840 ± 0.0001 and 0.4836 ± 0.0001 in the Compton scattering intensity and 1.5903 ± 0.0016 and 1.5898 ± 0.0016 in the S-parameter, respectively. These values in the anode of the charged and discharged states are 0.4177 ± 0.0001 and 0.4155 ± 0.0001 in the Compton scattering intensity and 1.7802 ± 0.0016 and 1.7807 ± 0.0017 in the S-parameter, respectively. The distribution of the anode in the 0.37–0.4 regions in the Compton scattering intensity and the 1.6–2 regions in the S-parameter appears in the aged cell. This region is highlighted in orange dotted circles in these figures. As the lattice volume of the anode expanded with degradation, as shown in both the Compton scattering intensity and S-parameter distributions in Figure 4, a stable phase of the LiAl alloy is formed in the VL2020 cell by repeating the charge–discharge cycle. Here, the three possible alloys are AlLi, Al₂Li₃, and Al₄Li₉ in the Al–Li binary diagram [33]. Additionally, two phases of β -AlLi and AlLi_{2-x} are also confirmed experimentally [34]. As a result, the distributions that are shown in the orange dotted circles in Figure 5c,d appeared. The region with low Compton scattering intensity and a high S-parameter value near the interface between the cathode and separator in Figure 4 corresponds to the 0.2–0.3 regions in the Compton scattering intensity and to 2.3–2.8 in the S-parameter values in Figure 5c,d. This region is highlighted

in the blue dotted circles in these figures. A possible reason for this distribution appearing near the surface of the separator on the aged cell is the electrolyte decreasing due to the generated microbubbles.

We estimated the porosity of the separator in the aged cell from the electron density because the Compton scattering intensity is proportional to the electron density as shown in Equation (1). The electron density ρ_e was calculated as:

$$\rho_e = \frac{N_A \cdot \rho}{M}, \quad (6)$$

where N_A is the Avogadro constant. ρ is the density of the separator in the fresh cell, and the value is 0.6956 g/cm³. ρ was obtained by measuring the weight and size of the separator using the electric balance after drying by pulling it out from the fresh cell. M is the atomic weight. The atomic weight of 42.078 in the polypropylene is used as the separator. The obtained ρ_e of the separator is 9.9548×10^{21} cm⁻³, and we assume the porosity at 100%. Then, the electron density of the separator, which includes 23% of the dimethoxyethane (the atomic weight is 90.118) electrolyte is calculated as the measured polypropylene density (0.6956 g/cm³) is small, approximately 77% compared with the theoretical polypropylene density (0.905 g/cm³). This value is 1.1298×10^{22} cm⁻³, and we assume the porosity at 0%. The averaged Compton scattering intensities of the separator in the discharged fresh and aged cells are 0.3538 ± 0.0001 and 0.3146 ± 0.0001 , respectively. When the Compton scattering intensity of the separator in the fresh cell is assumed with a porosity of 0%, the porosity of the separator in the aged cell is approximately 93.2%. As the Compton scattering intensity from vacancy is weak, this considers that the vacancy is introduced in the separator by the degradation of the cell. From the above, the degradation mechanism of the VL2020 cell is that first, the stable phase of the anode is formed by the overvoltage cycle, then the appearance of the microbubbles is induced by the decomposition of the electrolyte [35] as lithium reactions with the cycle are prevented by the formation of the stable phase of the anode.

In this study, by combining Compton scattering intensity and S-parameter analysis, we non-destructively quantified the lithium composition and identified the degradation mechanism of the commercial VL2020 cell. These Compton scattering imaging features are expected to be useful as a novel non-destructive analysis of commercialized lithium rechargeable cells.

4. Conclusions

We apply synchrotron-based high-energy X-ray Compton scattering imaging to fresh and aged commercialized coin-type VL2020 cells to identify the degradation mechanisms. The fresh cell shows clear variations in the charged and discharged states via the Compton scattering intensity and S-parameter, and we observe a structural change with the volume expansion of the anode. On the other hand, the aged cell no longer shows the variation for the charge and discharge states. From the correlation between the Compton scattering intensity and S-parameter, we find that the stable phase of the anode formed through the overvoltage charge–discharge cycles. This stable phase prevents lithium reactions and produces the appearance of microbubbles with the decomposition of the electrolyte.

Author Contributions: Conceptualization, K.S., Y.S., and H.S.; methodology, K.S., Y.O., and N.T.; software, K.S. and Y.O.; validation, all authors; formal analysis, K.S., Y.O., K.H., and H.S.; investigation, K.S. and N.T.; resources, K.S., N.T., and Y.S.; data curation, K.S.; writing, original draft preparation, K.S.; writing, review and editing, all authors; visualization, K.S., Y.O., K.H., and H.S.; supervision, H.S.; project administration, H.S.; funding acquisition, K.S. All authors read and agreed to the published version of the manuscript.

Funding: This research was funded by The Futaba Foundation and partially supported by MEXT KAKENHI Grant No. 19K05519 and the Japan-UK Research Cooperative Program between JSPS and The Royal Society.

Acknowledgments: Compton scattering experiments were performed with the approval of JASRI (Proposal Nos. 2017B1360, 2018A1320, and 2019B1668).

Conflicts of Interest: The authors declare no conflict of interest.

References

1. Zubi, G.; Dufo-López, R.; Carvalho, M.; Pasaoglu, G. The lithium-ion battery: State of art and future perspectives. *Renew. Sustain. Energy Rev.* **2018**, *89*, 292–308. [[CrossRef](#)]
2. Lin, F.; Liu, Y.; Yu, X.; Cheng, L.; Singer, A.; Shpyko, O.G.; Xin, H.L.; Tamura, N.; Tian, C.; Weng, T.; et al. Synchrotron X-ray Analytical Techniques for Studying Materials Electrochemistry in Rechargeable Batteries. *Chem. Rev.* **2017**, *117*, 13123–13186. [[CrossRef](#)]
3. Li, Y.; Li, Y.; Pei, A.; Yan, K.; Sun, Y.; Wu, C.L.; Joubert, L.M.; Chin, R.; Koh, A.L.; Yu, Y.; et al. Atomic structure of sensitive battery materials and interfaces revealed by cryo-electron microscopy. *Science* **2017**, *358*, 506–510. [[CrossRef](#)] [[PubMed](#)]
4. Zachman, M.J.; Tu, Z.; Choudhury, S.; Archer, L.A.; Kourkoutis, L.F. Cryo-STEM mapping of solid-liquid interfaces and dendrites in lithium-metal batteries. *Nature* **2018**, *560*, 345–349. [[CrossRef](#)] [[PubMed](#)]
5. Kumar, V.; Yong Sheng Eng, A.; Wang, Y.; Nguyen, D.T.; Ng, M.F.; Seh, Z.W. An artificial metal-alloy interphase for high-rate and long-life sodium-sulfur batteries. *Energy Storage Mater.* **2020**, *29*, 1–8. [[CrossRef](#)]
6. Kumar, V.; Wang, Y.; Yong Sheng Eng, A.; Ng, M.F.; Seh, Z.W. A Biphasic Interphase Design Enabling High Performance in Room Temperature Sodium-Sulfur Batteries. *Cell Rep. Phys. Sci.* **2020**, *1*, 100044. [[CrossRef](#)]
7. Harding, G.; Harding, E. Compton scatter imaging: A tool for historical exploration. *Appl. Radiat. Isotop.* **2010**, *68*, 993–1005. [[CrossRef](#)]
8. Redler, G.; Jones, K.C.; Templeton, A.; Bernard, D.; Turian, J.; Chu, J.C.H. Compton scatter imaging: A promising modality for imaging guidance in lung stereotactic body radiation therapy. *Med. Phys.* **2018**, *45*, 1233–1240. [[CrossRef](#)]
9. Liu, Y.; Xiong, X.; Zhang, Z.; Shuai, L.; Wang, X.; Zhou, W.; Wang, C.; Wei, L. A novel method of coded-aperture push-broom Compton scatter imaging: Principles, simulations and experiments. *Nucl. Instrum. Methods Phys. Res.* **2019**, *A940*, 30–39. [[CrossRef](#)]
10. Itou, M.; Orikasa, Y.; Gogyo, Y.; Suzuki, K.; Sakurai, H.; Uchimoto, Y.; Sakurai, Y. Compton scattering imaging of a working battery using synchrotron high-energy X-rays. *J. Synchrotron Radiat.* **2015**, *22*, 161–164. [[CrossRef](#)]
11. Suzuki, K.; Barbiellini, B.; Orikasa, Y.; Kaprzk, S.; Itou, M.; Yamamoto, K.; Wang, Y. J.; Hafiz, H.; Uchimoto, Y.; Bansil, A.; et al. Non-destructive measurement of in-operando lithium concentration in batteries via x-ray Compton scattering. *J. Appl. Phys.* **2016**, *119*, 025103. [[CrossRef](#)]
12. Suzuki, K.; Suzuki, A.; Ishikawa, T.; Itou, M.; Yamashige, H.; Orikasa, Y.; Uchimoto, Y.; Sakurai, Y.; Sakurai, H. In operando quantitation of Li concentration for a commercial Li-ion rechargeable battery using high-energy X-ray Compton scattering. *J. Synchrotron Radiat.* **2017**, *24*, 1006–1011. [[CrossRef](#)]
13. Suzuki, K.; Kanai, R.; Tsuji, N.; Yamashige, H.; Orikasa, Y.; Uchimoto, Y.; Sakurai, Y.; Sakurai, H. Dependency of the Charge-Discharge Rate on Lithium Reaction Distributions for a Commercial Lithium Coin Cell Visualized by Compton Scattering Imaging. *Condens. Matter* **2018**, *3*, 27. [[CrossRef](#)]
14. Suzuki, K.; Honkanen, A.-P.; Tsuji, N.; Jalkanen, K.; Koskinen, J.; Morimoto, H.; Hiramoto, D.; Terasaka, A.; Hafiz, H.; Sakurai, Y.; et al. High-Energy X-Ray Compton Scattering Imaging of 18650-Type Lithium-Ion Battery Cell. *Condens. Matter* **2019**, *4*, 66. [[CrossRef](#)]
15. Chen, D.; Yi, R.; Chen, S.; Xu, T.; Gordin, M.L.; Lv, D.; Wang, D. Solvothermal synthesis of V₂O₅/graphene nanocomposites for high performance lithium ion batteries. *Mater. Sci. Eng. B* **2014**, *185*, 7–12. [[CrossRef](#)]
16. Liang, X.; Gao, G.; Du, Y.; Wang, J.; Sun, W.; Liu, Y.; Zhang, K.; Wu, G. Synthesis and characterization of various V₂O₅ microsphere structures and their electrochemical performance. *J. Alloys Compd.* **2018**, *757*, 177–187. [[CrossRef](#)]
17. Liu, P.; Zhu, K.; Bian, K.; Xu, Y.; Zhang, F.; Zhang, W.; Zhang, J.; Huang, W. 3D hierarchical porous sponge-like V₂O₅ micro/nano-structures for high-performance Li-ion Batteries. *J. Alloys Compd.* **2018**, *765*, 901–906. [[CrossRef](#)]
18. Wang, H.; Bai, Y.; Chen, S.; Luo, X.; Wu, C.; Lu, J.; Amine, K. Binder-Free V₂O₅ Cathode for Greener Rechargeable Aluminum Battery. *ACS Appl. Mater. Interfaces* **2015**, *7*, 80–84. [[CrossRef](#)]
19. Mukherjee, A.; Sa, N.; Phillips, P.J.; Burrell, A.; Vaughey, J.; Klie, R.F. Direct Investigation of Mg Intercalation into the Orthorhombic V₂O₅ Cathode Using Atomic-Resolution Transmission Electron Microscopy. *Chem. Mater.* **2017**, *29*, 2218–2226. [[CrossRef](#)]

20. Guo, H.; Hou, G.; Li, D.; Sun, Q.; Ai, Q.; Si, P.; Min, G.; Lou, J.; Feng, J.; Ci, L. High Current Enabled Stable Lithium Anode for Ultralong Cycling Life of Lithium-Oxygen Batteries. *ACS Appl. Mater. Interfaces* **2019**, *11*, 30793–30800. [[CrossRef](#)]
21. Sharaf, J. M. Practical aspects of Compton scatter densitometry. *Appl. Radiat. Isotop.* **2001**, *54*, 801–809. [[CrossRef](#)]
22. Holt, R.S.; Cooper, M.J.; Jackson, D.J. Gamma-ray scattering techniques for non-destructive testing and imaging. *Nucl. Instrum. Methods* **1984**, *221*, 98–104. [[CrossRef](#)]
23. Biggs, F.; Mendelson, L.B.; Mann, J.B. Hartree-Fock Compton profiles for the elements. *At. Data Nucl. Data Tables* **1975**, *16*, 201. [[CrossRef](#)]
24. Schülke, W. The theory of Compton scattering. In *X-ray Compton Scattering*, 1st ed.; Cooper, M.J., Mijnenrends, P.E., Shiotani, N., Sakai, N., Bansil, A., Eds.; Oxford University Press: Oxford, UK, 2004; pp. 22–81.
25. Barbiellini, B. A natural orbital method for the electron momentum distribution in mater. *J. Phys. Chem. Solids* **2000**, *61*, 341–344. [[CrossRef](#)]
26. Barbiellini, B.; Bansil, A. Treatment of correlation effects in electron momentum density: Density functional theory and beyond. *J. Phys. Chem. Solids* **2001**, *62*, 2181–2189. [[CrossRef](#)]
27. Suzuki, K.; Barbiellini, B.; Orikasa, Y.; Go, N.; Sakurai, H.; Kaprzyk, S.; Itou, M.; Yamamoto, K.; Uchimoto, Y.; Wang, Y.J.; et al. Extracting the Redox Orbitals in Li Battery Materials with High-Resolution X-ray Compton Scattering Spectroscopy. *Phys. Rev. Lett.* **2015**, *114*, 087401. [[CrossRef](#)]
28. Barbiellini, B.; Suzuki, K.; Orikasa, Y.; Kaprzyk, S.; Itou, M.; Yamamoto, K.; Wang, Y.J.; Hafiz, H.; Yamada, R.; Uchimoto, Y.; et al. Identifying a descriptor for d-orbital delocalization in cathodes of Li batteries based on x-ray Compton scattering. *Appl. Phys. Lett.* **2016**, *109*, 073102. [[CrossRef](#)]
29. Hafiz, H.; Suzuki, K.; Barbiellini, B.; Orikasa, Y.; Callewaert, V.; Kaprzyk, S.; Itou, M.; Yamamoto, K.; Yamada, R.; Uchimoto, Y.; et al. Visualizing redox orbitals and their potentials in advanced lithium-ion battery materials using high-resolution X-ray Compton scattering. *Sci. Adv.* **2017**, *3*, e1700971. [[CrossRef](#)]
30. Hafiz, H.; Suzuki, K.; Barbiellini, B.; Orikasa, Y.; Kaprzyk, S.; Tsuji, N.; Yamamoto, K.; Terasaka, A.; Hoshi, K.; Uchimoto, Y.; et al. Identification of ferrimagnetic orbitals preventing spinel degradation by charge ordering in $\text{Li}_x\text{Mn}_2\text{O}_4$. *Phys. Rev. B* **2019**, *100*, 205104. [[CrossRef](#)]
31. Morales, J.; Trócoli, R.; Franger, S.; Santos-Peña, J. Cycling-induced stress in lithium ion negative electrodes: LiAl/LiFePO_4 and $\text{Li}_4\text{Ti}_5\text{O}_{12}/\text{LiFePO}_4$ cells. *Electrochim. Acta* **2010**, *55*, 3075–3082. [[CrossRef](#)]
32. Hamon, Y.; Brousse, T.; Joysse, F.; Topart, P.; Buvat, P.; Schleich, D.M. Aluminum negative electrode in lithium ion batteries. *J. Power Sources* **2001**, *97–98*, 185–187. [[CrossRef](#)]
33. McAlister, A.J. The Al-Li (Aluminum-Lithium) system. *Bull. Alloy. Phase Diagr.* **1982**, *3*, 177. [[CrossRef](#)]
34. Ghavidel, M.Z.; Kupsta, M.R.; Le, J.; Feygin, E.; Espitia, A.; Fleischauer, M.D. Electrochemical Formation of Four Al-Li Phases ($\beta\text{-AlLi}$, Al_2Li_3 , AlLi_{2-x} , Al_4Li_9) at Intermediate Temperatures. *J. Electrochem. Soc.* **2019**, *166*, A4034–A4040. [[CrossRef](#)]
35. Chen, X.; Hou, T.Z.; Li, B.; Yan, C.; Zhu, L.; Cheng, B.; Peng, H.J.; Huang, J.Q.; Zhang, Q. Towards stable lithium-sulfur batteries: Mechanistic insights into electrolyte decomposition on lithium metal anode. *Energy Storage Mater.* **2017**, *8*, 194–201. [[CrossRef](#)]

